Which long-baseline neutrino experiments are preferable?

V. Barger,[1,*] P. Huber,[1,†] D. Marfatia,[2,‡] and W. Winter[3,§]

[1]*Department of Physics, University of Wisconsin, Madison, Wisconsin 53706, USA*
[2]*Department of Physics & Astronomy, University of Kansas, Lawrence, Kansas 66045, USA*
[3]*Institut für theoretische Physik und Astrophysik, Universität Würzburg, D-97074 Würzburg, Germany*

We discuss the physics of superbeam upgrades, where we focus on T2KK, a NuMI beam line based experiment NOνA*, and a wide-band beam (WBB) experiment independent of the NuMI beam line. For T2KK, we find that the Japan-Korea baseline helps resolve parameter degeneracies, but the improvement due to correlated systematics between the two detectors (using identical detectors) is only moderate. For an upgrade of NOνA with a liquid argon detector, we demonstrate that the Ash River site is preferred compared to alternatives, such as at the second oscillation maximum, and is the optimal site within the U.S. For a WBB experiment, we find that high proton energies and long decay tunnels are preferable. We compare water Cherenkov and liquid argon technologies, and find the break-even point in detector cost at about 4:1. In order to compare the physics potential of the different experimental configurations, we use the concept of *exposure* to normalize the performance. We find that experiments with WBBs are the best experimental concept. NOνA* could be competitive with sufficient luminosity. If $\sin^2 2\theta_{13} > 0.01$, a WBB experiment can perform better than a neutrino factory.

　　　　　　　　　　　　　　　　　　　PACS numbers: 14.60.Pq

I. INTRODUCTION

The motivation for measuring all the parameters of the neutrino mass matrix is that such knowledge will allow us to sift through the many neutrino mass models available [1] and lead us to a better understanding of the origin of neutrino masses.

To make further progress in our exploration of the neutrino sector, precision experiments are needed. The MINOS experiment [2] will provide an accurate determination of $|\Delta m_{31}^2|$ in the near future [3,4]. Reactor experiments with multiple detectors, like the Double CHOOZ [5] and Daya Bay [6] experiments, will either constrain the angle θ_{13} (which mixes the solar and atmospheric oscillation scales) from above, or from below if $\sin^2 2\theta_{13}$ is larger than about 0.03 [7]. Also, the Tokai-to-Kamioka (T2K) experiment [8] which is under construction, and expected to be in operation in a couple of years, will detect $\nu_\mu \to \nu_e$ oscillations if θ_{13} is favorably large, but due to its relatively short baseline will not be sensitive to the neutrino mass hierarchy. While the reactor and T2K experiments will provide important guidance about θ_{13}, they are inherently limited in their abilities to determine the mass hierarchy and to tell us if the *CP* symmetry is broken in the lepton sector. For these measurements, upgraded experiments with neutrino beams are necessary. See Ref. [9] for a review.

In this paper, we discuss upgraded experiments with high intensity neutrino beams resulting from proton beams with target powers above 1 MW that are directed towards either very large or very sophisticated detectors. We compare the potential of these experiments with that of a neutrino factory and a β-beam experiment. Our discussion, in the usual parlance, is that of a ''phase II'' program, and is addressed to experts.

The goals of our study are
(1) To determine for the Tokai-to-Kamioka-and-Korea (T2KK) experiment [10–12] (consisting of two identical detectors of half the size as the originally envisaged megaton-scale detector)
    (a) the effect of placing half the fiducial mass at the 1050 km baseline compared to having all the fiducial mass at 295 km (see Sec. III B),
    (b) and how it helps that the two detectors are identical, i.e., that the systematics are fully correlated (see Sec. III C).
(2) To determine the optimal location for a second detector in an upgraded NuMI off-axis experiment, which we dub NOνA*. See Secs. IV B and IV C.
(3) To determine the optimal baseline, proton energy, and decay tunnel length for a Fermilab-based wide-band beam. See Secs. V B and V C.
(4) To compare the setups of different proposed superbeam experiments on an equal footing by expressing their sensitivities as functions of exposure, as in Ref. [13], and to assess if it is better to place a detector on axis or off axis. See Sec. VI A.
(5) To quantify the robustness of our conclusions under variations of exposure, systematics, and the value of $|\Delta m_{31}^2|$. See Sec. VI B.
(6) To determine the smallest value of θ_{13} for which superbeam experiments are competitive with a neutrino factory or a β-beam experiment. See Sec. VI C.

*barger@physics.wisc.edu
†phuber@physics.wisc.edu
‡marfatia@ku.edu
§winter@physik.uni-wuerzburg.de

II. ANALYSIS TECHNIQUES

There is an eightfold degeneracy [14] in the determination of the oscillation parameters that arises from three twofold degeneracies [14–17]:

(i) Intrinsic $(\theta_{13}, \delta_{CP})$ degeneracy with $(\theta_{13}, \delta_{CP}) \rightarrow (\theta'_{13}, \delta'_{CP})$.

(ii) Sign degeneracy with $\Delta m_{31}^2 \rightarrow -\Delta m_{31}^2$.

(iii) Octant degeneracy with $\theta_{23} \rightarrow \pi/2 - \theta_{23}$.

The octant degeneracy will not influence our results and discussions since we set the true value for the atmospheric mixing angle to the current best-fit value $\sin^2 2\theta_{23} = 1$. The intrinsic degeneracy is very often not explicitly present (as a disconnected degenerate solution) for superbeams, but it appears as a strong correlation (connected degenerate solutions). In most cases, the sign degeneracy affects the performance. For example, the *CP*-conserving solutions of the wrong-hierarchy solution may destroy the *CP* violation (CPV) sensitivity because *CP* conservation cannot be excluded. Longer baselines and therefore strong matter effects [18] may help to resolve this degeneracy and to improve the physics performance, because they may intrinsically separate the different hierarchy solutions; see, e.g., Refs. [14,16,19–22] for a pictorial representation in terms of bi-probability diagrams. Therefore, a detector located at a sufficiently long baseline is usually a key element of any superbeam upgrade to break the remaining degeneracy.

In order to reduce correlations, especially between θ_{13} and δ_{CP}, different strategies are possible for superbeam upgrades. For experiments using the off-axis technology, a second detector at a different location can provide complementary information for a different L and/or E. In addition, better energy resolution and higher statistics may provide measurements of the transition probability for different values of E. Alternatively, a wide energy spectrum can provide these measurements even with a rather poor energy resolution. In this study, we discuss several very different such approaches and demonstrate how these strategies affect the physics performance.

For the quantitative analysis, we use the GLOBES software [23,24]. As input, or so-called true values, we use, unless stated otherwise (see Refs. [25,26]),

$$\Delta m_{31}^2 = 2.5 \times 10^{-3} \text{ eV}^2, \qquad \sin^2 \theta_{23} = 0.5,$$
$$\Delta m_{21}^2 = 8.0 \times 10^{-5} \text{ eV}^2, \qquad \sin^2 \theta_{12} = 0.3, \qquad (1)$$

where $\sin^2 2\theta_{13} \lesssim 0.1$. In anticipation of near future experiments, we assume a 4% external measurement of solar oscillation parameters (see, e.g., Refs. [27,28]), a 10% measurement of the atmospheric parameters (see, e.g., Refs. [4,29]), and include matter density uncertainties of the order of 5% [30,31] uncorrelated between different baselines.

In order to make an unbiased comparison of the physics potentials of the experimental setups, we will in some cases consider their sensitivities as functions of *exposure* [13],

$$\mathcal{L} = \text{detector mass (Mt)} \times \text{target power (MW)}$$
$$\times \text{running time } (10^7 \text{ s}). \qquad (2)$$

The exposure is a measure of the integrated luminosity. For the Fermilab-based experiments, we use 1.7×10^7 seconds uptime per year, and for T2KK, we use 10^7 seconds uptime per year (as per the corresponding documents).

III. T2KK: AN OFF-AXIS EXPERIMENT WITH TWO IDENTICAL DETECTORS

T2KK is a Japanese-Korean approach for a superbeam upgrade of the T2K off-axis superbeam experiment [8]. Originally, it was planned to upgrade T2K to T2HK (Tokai-to-HyperKamiokande) with a 4 MW proton beam and a megaton-size water Cherenkov detector. Recently, it was recognized that placing a part of the detector mass in Korea would enhance the mass hierarchy and degeneracy resolution potential [10–12]. In particular, it was emphasized in Ref. [10] that using identical detectors and the same off-axis angle would reduce the impact of systematics significantly. More recent studies have investigated the off-axis angle optimization and the splitting of the detector mass between the different sites [32,33]. However, in this case, the detectors cannot be assumed to be identical anymore in the sense that systematics are correlated between the two detectors. In this study, we focus on the setup with correlated detectors because this aspect is very specific to the T2KK idea and has certain characteristics.

A. Simulation details

Details of our simulation of T2KK including the beam spectrum, cross sections, and efficiencies are based on the setup "JHF-HK" from Ref. [34] with an off-axis angle of $2°$. In order to include the systematics correlation between the two detectors, we use the GLOBES software [23,24] which allows for user-defined systematics. For detector masses and running times, we follow Ref. [10]. We use four years of neutrino running, followed by four years of antineutrino running. We assume 52×10^{20} pot/yr in either mode corresponding to a target power of 4 MW. The (identical) water Cherenkov detectors of fiducial mass 270 kt will be located at a distance of 295 km and 1050 km with the same off-axis angle. According to our definition of the exposure [cf. Eq. (2)], this corresponds to $\mathcal{L} = 17.28 \text{ Mt MW } 10^7$ s. We follow Ref. [10] for the systematics modeling as well, i.e., we assume that the systematics are completely correlated between the two identical detectors in Japan and Korea, and the uncorrelated errors are small. We include the signal and background normalization errors of the appearance channels (typically 5% each), and allow for an independent 5%
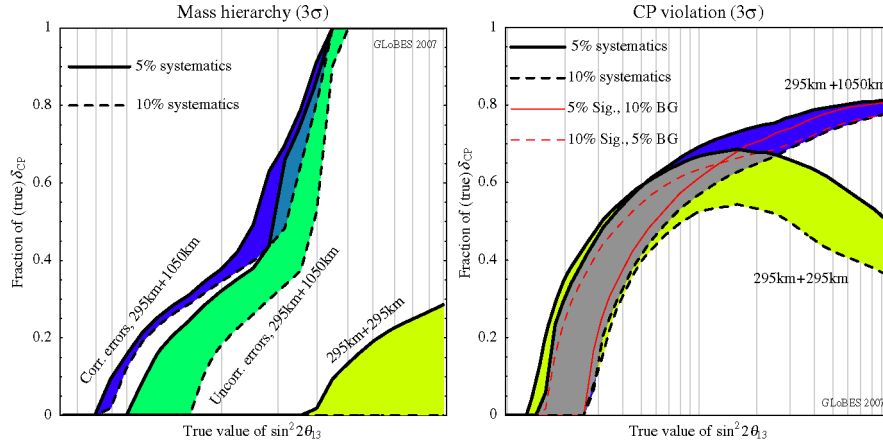
FIG. 1 (color online). Impact of systematics, Japan-Korea baseline, and detector correlation: 3σ sensitivity to the (normal) mass hierarchy and CP violation for T2KK as a function of $\sin^2 2\theta_{13}$ and the fraction of δ_{CP}; for a definition see Fig. 3 of Ref. [35]. In the figures, several different systematics options and baseline combinations are shown, where systematics refers to both signal and background normalization errors of the appearance channel. For the dark gray-shaded (blue) and light gray-shaded (yellow) regions, systematics are assumed to be fully correlated between the detectors, which corresponds to only one detector for the 295 km + 295 km option. For the medium gray-shaded region (left plot), systematics are assumed to be uncorrelated between two detectors. We do not show this region in the right plot, because it is almost identical to the dark-shaded (correlated) region. In both plots, regions of overlap have gray-scale shading intermediate to those of the overlapping regions. Note that we assumed neutrino and antineutrino systematics to be uncorrelated.

background energy calibration error. In addition, we include the disappearance channels with a 2.5% normalization uncertainty and a 20% background normalization uncertainty [34]. Note that we assume the errors to be completely correlated between the two detectors, but to be completely uncorrelated between the neutrino and antineutrino channels (as opposed to Ref. [10]). Our simulation uses the spectral information for the quasielastic (QE) charged-current (CC) events only (because the detector cannot measure the hadronic energy deposition for the non-QE events), and the total rate for all CC events.

B. Role of systematics correlation and second baseline

We present our main results in Fig. 1. This figure show the mass hierarchy and CP violation measurements for several systematics and baseline options, where the total detector mass is 0.27 Mt + 0.27 Mt. The "systematics" correspond to the signal and background normalization errors of the appearance channels, which we have determined to be the main impact factors.

A determination of the mass hierarchy will be difficult without the 1050 km baseline. As one can deduce from Fig. 1 (left panel), a large systematic error of 10% would even destroy the measurement completely for the short baseline only. However, for the combination of baselines, the impact of systematics is small (dark/blue region). We also show the curves for uncorrelated errors between the two detectors (medium gray/green region). Having identical detectors clearly helps for the mass hierarchy measurement. Not only is the absolute $\sin^2 2\theta_{13}$ reach better for correlated systematics, but also the impact of worse sys-

tematics becomes smaller. We have tested that a 2% systematic uncertainty would not substantially improve the results. It is the background normalization error which affects the results most because it dominates the measurement for small $\sin^2 2\theta_{13}$.

For CP violation, the situation is very different (cf. Fig. 1, right panel).[1] The long baseline helps to resolve the degeneracies for large $\sin^2 2\theta_{13}$, while for small $\sin^2 2\theta_{13}$ having all the detector mass at 295 km would be better because of the larger statistics. The impact of the absolute systematics is strong and is independent of the baseline combination. We do not show the curves for uncorrelated errors in the right panel of Fig. 1 because they overlap significantly with the correlated curves. This means that, while the longer baseline is clearly beneficial, the fact that the detectors are identical is not. It will be very important to control the systematics for CP violation measurements since the shorter baseline practically measures CP violation, and the systematics impact is largest between the uncorrelated neutrino and antineutrino errors. Note that the impact of different individual systematic uncertainties is illustrated by the gray curves in the right panel of Fig. 1.

---

[1]The fraction of (true values of) δ_{CP} for which an experiment is sensitive to CPV cannot be unity even for the best setup and very large $\sin^2 2\theta_{13}$. The reason is that one cannot establish CP violation at and around the CP-conserving values which one wants to discriminate from the CP-violating effect. Therefore, the fraction of δ_{CP} has to be smaller than 1 by definition. This indicator describes how close to CP conservation one can establish CP violation, i.e., how small CP-violating effects an experiment can find.

For small $\sin^2 2\theta_{13}$, the background normalization dominates, while for large $\sin^2 2\theta_{13}$ the signal normalization has the greatest impact.

C. Impact of degree of correlation

In order to compare our results with those of Ref. [10], we illustrate the impact of different degrees of correlation in Fig. 2. Systematics can be either fully uncorrelated between the two detectors and between neutrinos and antineutrinos (gray curves), fully correlated between the two detectors but uncorrelated between neutrinos and antineutrinos (black curves), or fully correlated between the two detectors and neutrinos and antineutrinos (dashed curves). We have chosen 5% signal and background normalization uncertainties. If there is some correlation between neutrino and antineutrino systematics, the *CP* violation measurement will especially be improved. In fact, we have tested that this correlation makes the *CP* violation sensitivity rather insensitive to the absolute magnitude of the systematic errors, whereas the correlation between the detectors hardly has any impact. The bands in Fig. 2 reflect all possible outcomes for 5% systematics depending on the achievable degree of correlation. For the rest of this study, we adopt the conservative point of view that systematics between the neutrino and antineutrino modes are uncorrelated (but correlated between the two detectors). Because they are operated at different times with different beams, the cross section errors are certainly uncorrelated, and the background reduction may also be different (e.g., at least the π^0 production rates are differ-

ent). In addition, the argument of some correlation between neutrino and antineutrino systematics could be applied to other experiments as well, and we treat all experiments with comparable assumptions. Eventually, note that, while correlated systematics between neutrinos and antineutrinos would increase the physics potential, it would relatively weaken the physics case for the Japan-Korea baseline because all detector mass at $L = 295$ km would be better for *CP* violation measurements at small $\sin^2 2\theta_{13}$ and improve the mass hierarchy potential, too.

In summary, we find that the 1050 km baseline clearly helps for both mass hierarchy and *CP* violation measurements regardless of the size of the systematic errors. However, it is only useful that the detectors are identical (and have completely correlated systematics) for the mass hierarchy measurement—as long as neutrino and antineutrino systematics are assumed to be uncorrelated. In addition, we have tested that matter density uncertainties and the assumptions for the solar parameter precisions practically do not have an impact. For the rest of this study, we use the standard T2KK setup with 5% systematics correlated between the two detectors but uncorrelated between the neutrino and antineutrino running; cf. Table II.

IV. NOνA*: A NEW EXPERIMENT BASED ON THE NUMI BEAM LINE

The first experiment based on the NuMI beam line at Fermilab was the MINOS experiment [39]. It has been proposed to use the NuMI beam line for a future off-axis
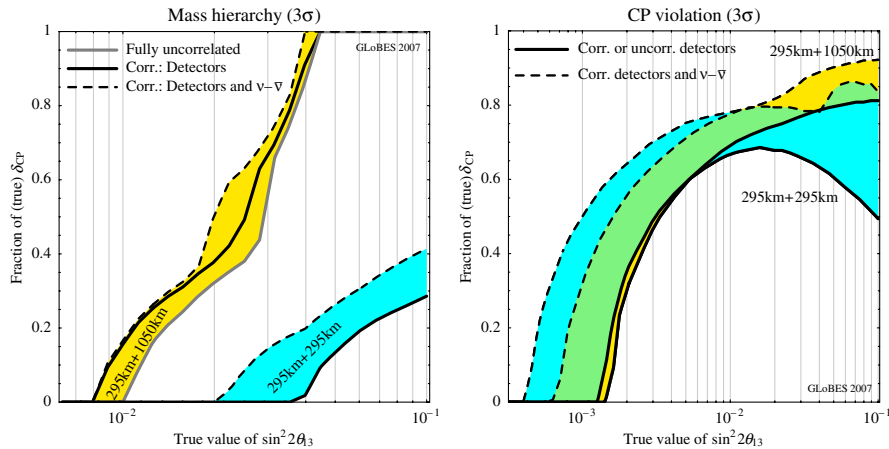

FIG. 2 (color online). Impact of detector versus neutrino-antineutrino correlation: 3σ sensitivity to the (normal) mass hierarchy and *CP* violation for T2KK as a function of $\sin^2 2\theta_{13}$ and the *CP* fraction. In the figures, several different systematics options and baseline combinations are shown. The systematics can be either fully uncorrelated between the two detectors and between neutrinos and antineutrinos (gray curves), fully correlated between the two detectors but uncorrelated between neutrinos and antineutrinos (black curves), or fully correlated between the two detectors and neutrinos and antineutrinos (dashed curves), where 5% signal and background normalization uncertainties are chosen for all curves. The bands reflect the possible outcome for 5% systematics depending on the achievable degree of correlation. Note that, in the right plot, the curves for fully uncorrelated detectors are practically identical to the black curves (not shown) and the region where the bands overlap have gray-scale shading intermediate to those of the overlapping bands. For the 295 km + 295 km option, the correlated detectors correspond to one detector with uncorrelated systematics.

superbeam experiment. The NuMI off-axis experiment (NOνA) was originally designed with a low-Z-tracking calorimeter to be placed off axis in the NuMI beam [40]. Since the then preferred baseline of $L \simeq 712$ km turned out to be too short to be complementary to the T2K experiment in Japan, longer baselines were suggested in Refs. [21,41–43].[2] As a rule of thumb,

$$\left(\frac{L}{E}\right)_{\text{NuMI}} \gtrsim \left(\frac{L}{E}\right)_{\text{T2K}} \qquad (3)$$

was found in order to yield synergistic physics, which translates to $L_{\text{NuMI}} \gtrsim 862$ km for $0.72°$ off-axis angle. Hence, a longer baseline, $L \simeq 810$ km to the Ash River site in Minnesota, has been proposed for the NOνA experiment [45]. A typical off-axis angle suggested is $0.85°$, corresponding to 12 km off axis at this baseline. In addition, a totally active scintillating detector (TASD) is the now accepted detector technology, often considered with a mass of 25 kt. Alternative sites with longer baselines in Canada (because of the beam geometry), such as Vermillion Bay, with potentially attractive physics potential are not actively being considered.

For upgrades of the NOνA experiment, several ideas have been proposed. Two approaches are discussed in the NOνA proposal [45]. The luminosity could be increased by using a proton driver [46], or a second detector could be placed at the second oscillation maximum at a short baseline $L = 710$ km with a larger off-axis angle, $2.4°$. We refer to this setup as "2nd maximum." In principle, increasing the protons on target has the same effect as increasing the detector mass at the same site. However, a different detector technology may allow for better energy resolution, background rejection, etc., which needs to be explored. Another possible upgrade is to use the same L/E for both detectors, an idea similar to that encapsulated in Eq. (3). Since longer baselines may not be possible with a detector within the U.S., a larger off-axis angle of $2.4°$ combined with a short baseline $L \simeq 200$ km, called "Super-NOνA," was suggested in Refs. [47,48]. In this section, we investigate the issue of site optimization using a liquid argon detector as a second detector. Note that, for the NuMI-based experiment, no new beam line is needed, but the existing beam line constrains the combinations of allowed baselines and off-axis angles.

A. Simulation details

Our simulation of the NOνA experiment is based on that in Ref. [43] updated with the numbers from Ref. [45]. We assume 10^{21} protons on target per year, corresponding to a thermal target power of 1.13 MW (for both the neutrino and antineutrino modes), which may be achieved in the Super-NuMI phase at Fermilab [49]. For phase I, we

assume a 25 kt TASD located at a baseline of 810 km and $0.85°$ (12 km) off axis.[3] The fluxes for phase I are taken from [50]. This location corresponds to the Ash River site. For the running times, we assume three years of neutrino running and three years of antineutrino running, followed by another period of three years of neutrino running and three years of antineutrino running, i.e., 12 years of operation altogether. For phase II, which we refer to as NOνA*, we assume a 100 kt liquid argon time projection chamber (LArTPC) operated with the same proton luminosity for three years of neutrino running, followed by three years of antineutrino running. Since the optimization of the site for the second detector is our primary goal in this section, we do not choose a specific detector location. For the LArTPC simulation [51], we assume an overall signal efficiency of 0.8. The energy response of a LArTPC depends on the event type. Since the type of event can be unambiguously determined, we split the event sample into QE events, which have an energy resolution of $5\%/\sqrt{E}$, and all other CC events, which have a $20\%/\sqrt{E}$ energy resolution. We furthermore assume that all neutral-current (NC) events will be identified as such, which means that only the beam intrinsic ν_e's and $\bar{\nu}_e$'s remain as backgrounds. We adopt the NuMI beam fluxes for the low-energy option from Ref. [50], and we use the interpolation routines provided together with the fluxes to obtain the flux at any site. The interpolation errors are smaller than 10% [50] and should not impact our results. The systematic errors are assumed to be 5% for the signal and background normalizations.

B. Optimal detector location for NOνA*

In Fig. 3, we show the result of the optimization of the NOνA* detector location (with phase I at Ash River) for a relatively wide range of angles and baselines. For this plot we computed the sensitivity on a grid of 45 values in the off-axis angle from $0°$ to $5°$ and 45 values in the baseline from 100 km to 1250 km. The plots show a "conservative" $\log_{10}(\sin^2 2\theta_{13})$ reach at the 3σ C.L. for nonzero $\sin^2 2\theta_{13}$ (left column), CP violation (middle column), and normal mass hierarchy (right column) discovery potentials. The bold plus signs mark the locations with the best sensitivities. In some cases there is a gap in the sensitivity as a function of $\sin^2 2\theta_{13}$, i.e., the $\Delta\chi^2$ function assumes the value 9 (which corresponds to the 3σ C.L.) at more than one value of $\sin^2 2\theta_{13}$. In these cases, the conservative reach is defined as the largest $\sin^2 2\theta_{13}$ for which $\Delta\chi^2 = 9$. The upper row corresponds to (the simulated) $\delta_{CP} = -90°$, the lower row to $\delta_{CP} = +90°$.

For $\delta_{CP} = +90°$ (lower row), the Ash River location for the second detector is indeed optimal for $\sin^2 2\theta_{13}$ and CP

---

[2]In principle, one can also adjust the off-axis angle instead [44] in order to adjust the energy.

[3]The very specific detector mass of phase I does not affect our results, because phase I is only used for the optimization of the phase II detector location. We do not expect a major impact of a smaller phase I detector on the optimization discussion.
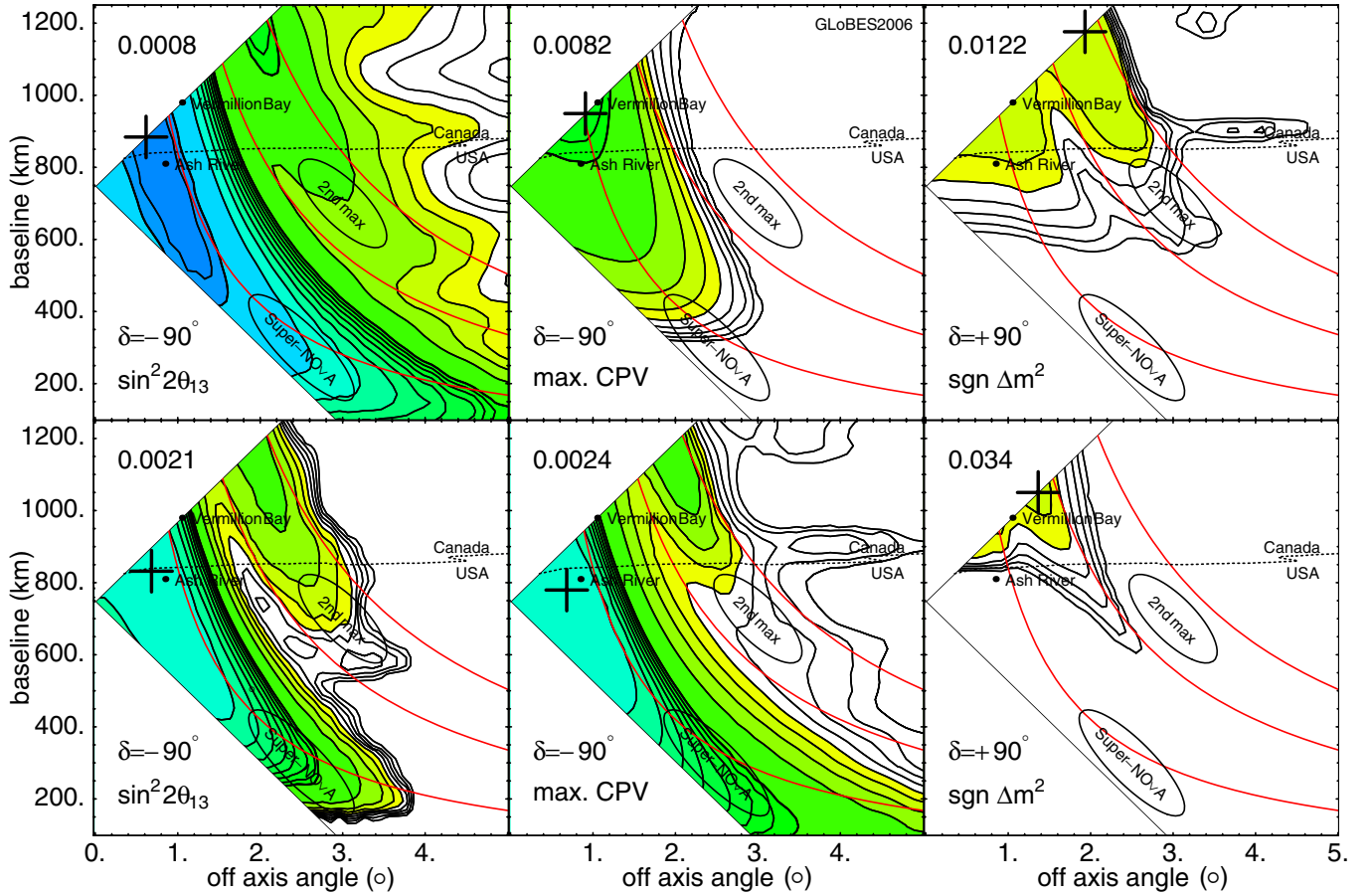
FIG. 3 (color online). Optimization of the NOνA* detector location (including phase I at Ash River) in the off-axis angle-baseline plane. The plots show the 3σ discovery reaches for nonzero $\sin^2 2\theta_{13}$, maximal CP violation, and the normal mass hierarchy. The bold plus signs mark the locations with the best sensitivity. These best sensitivities are given as numbers in the upper left corner of each panel. The thin black contours are logarithmically spaced in $\sin^2 2\theta_{13}$, i.e. $1, 2, \ldots, 9 \times 10^n$, where n ranges from -4 to -2. The color shading ranges from blue/dark (best) to green/light (worst); the bold contours correspond to $\sin^2 2\theta_{13} = 10^{-3}$ and 10^{-2}. The solid thin red curves are iso-L/E lines for the first, second, and third oscillation nodes. The dots correspond to specific selected sites. The dashed curve denotes the U.S.-Canadian border. The region below this curve is within the U.S.

violation. Relatively short baselines around $200-400$ km perform reasonably well, too. The Super-NOνA setup is marked in the figure by an ellipse with a corresponding label. A detector at the second oscillation maximum has poor sensitivity because of low event rates. The general region where such a second maximum detector could be located is marked by an ellipse taken from Refs. [45,52] with a corresponding label. Note that our iso-L/E line which corresponds to the second oscillation node does not intersect the region delimited by the ellipse. For the mass hierarchy sensitivity, however, a longer baseline is necessary. For $\delta_{CP} = -90°$ (upper row), the conclusions are similar for the Ash River site, but the Super-NOνA configuration performs worse for CP violation. The reason for the poor mass hierarchy performance of all short baseline sites for $\delta_{CP} = +90°$ is that the sign-degeneracy problem is most severe for this value of the CP phase. As far as the optimal off-axis angle is concerned, we assume that NC backgrounds can be identified with a

LArTPC. Therefore, in principle, an on-axis operation would be possible. However, since the intrinsic beam background is larger there, the exact on-axis position is not preferred.

C. Risk minimization

Two questions arise from Fig. 3:
(1) Is it possible to find one site which is a reasonable compromise for both cases of the CP phase?
(2) Is it possible to fix a site given the current uncertainty on the precise value of $|\Delta m_{31}^2|$?

Concerning the dependence of the optimal position on the true value of δ_{CP}, we observe that, for the discovery of nonzero $\sin^2 2\theta_{13}$, the optimal point does not move very much and is very close to Ash River. For CP violation, the difference in optimal positions is somewhat larger, but nevertheless the two points are close. Only for the mass hierarchy does the difference become considerable.

In order to address this issue in a more quantitative way, we define a *relative sensitivity reach* (RSR): For each of the six panels in Fig. 3, we divide the sensitivity reach at each point by its value at the best point (bold plus symbol), and thus RSR ≥ 1. The optimal value of RSR is unity. Next, the maximal RSR for the cases $\delta_{CP} = +90°$ and $\delta_{CP} = -90°$ for each point in the plane is determined. This "maximal RSR" corresponds to the risk-minimized optimum over the two different values of δ_{CP}. To illustrate this procedure, suppose that the maximum of the RSRs at a point is 1.2. At this point, the sensitivity reach would be within 20% of its optimal value for either case of $\delta_{CP} = \pm 90°$. The next step is to find the point which has the best maximal RSR for each measurement, i.e., the smallest maximal RSR value. This point corresponds to the optimal detector location given the risk minimization over $\delta_{CP} = \pm 90°$.

In order to discuss the dependence on the unknown Δm_{31}^2, we show in Fig. 4 the optimal detector locations for three different choices of Δm_{31}^2 as the small plus symbols. Let us first focus on these small plus symbols. The leftmost plusses in each panel are for $\Delta m_{31}^2 = 3.0 \times 10^{-3}$ eV^2, the middle ones are for our standard value $\Delta m_{31}^2 = 2.5 \times 10^{-3}$ eV^2, and the rightmost ones are for $\Delta m_{31}^2 = 2.0 \times 10^{-3}$ eV^2. The numbers next to each small plus symbol indicate the value of the maximal RSR at the points. We observe that for the measurement of $\sin^2 2\theta_{13}$ (left panel) and *CP* violation (middle panel) the maximal RSR never gets larger than 1.11 for any choice of Δm_{31}^2. Moreover, the optima are not very sensitive to Δm_{31}^2. For the mass hierarchy (right panel), however, the situation is less favorable. The optimal points are far apart, and for a higher value of Δm_{31}^2 it is impossible to find a location that has good sensitivity for both cases of $\delta_{CP} = \pm 90°$; the maximum RSR is 2.44.

We then risk-minimize over δ_{CP} and Δm_{31}^2. The contours shown in Fig. 4 are contours of constant RSR risk-minimized over the two values of δ_{CP} and the three values of Δm_{31}^2, i.e., the RSR value is maximized. Therefore, these help to find the optimum location for each measurement which takes into account our limited knowledge of the oscillation parameters. The bold plus symbols denote the risk-minimized detector locations. The maximal RSR values there are given in the upper left corner of each panel. Again, for the discovery of $\sin^2 2\theta_{13}$ and *CP* violation, we find that the values can be as low as 1.25 and that the two optima are not very far apart. This suggests that a joint optimization for these two measurements is indeed possible, even if one takes into account the large variation in Δm_{31}^2. The joint optimization results in a baseline $L = 880$ km at an off-axis angle 0.6°. For the mass hierarchy, the situation is more difficult, but clearly the main issue is not so much the uncertainty in $|\Delta m_{31}^2|$ (which will be considerably reduced by MINOS and NOνA phase I), but the fact that the *CP* phase will most likely be unknown at the time of the experiment. In this case, the optimal location is at $L = 930$ km and an off-axis angle 0.8°.

Further details on the optimization of the location of the NOνA* detector are provided in the Appendix.

For all setups considered here we have assumed an equal fraction of neutrino and antineutrino running. We have checked that this provides superior sensitivities for all
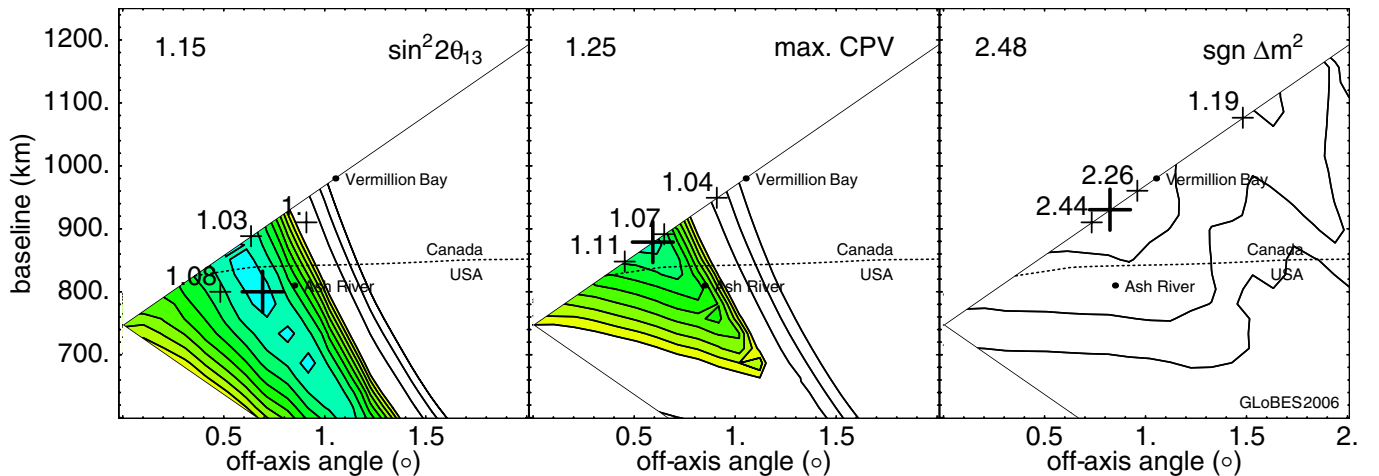

FIG. 4 (color online). Contours of constant maximum relative sensitivity reach (RSR) risk-minimized over $\delta_{CP} = \pm 90°$ and three values of $\Delta m_{31}^2 = (2.0, 2.5, 3.0) \times 10^{-3}$ eV^2. The shading ranges from 1.0 (blue/dark) to 2.0 (green/light) and the contours within the shading are in RSR steps of 0.1. The contours in the unshaded area are in steps of 1.0 extending up to 5. The bold plus symbols denote the points where the smallest values occur. The absolute optimum is given as the number in the upper left corner of each panel. The small plusses denote the points at which the optimum value of the maximum RSR occurs for one specific value of Δm_{31}^2 only. The leftmost (rightmost) plus sign corresponds to $\Delta m_{31}^2 = 3 \times 10^{-3} (2 \times 10^{-3})$ eV^2. The number adjacent to each plus sign is the value at the optimum. The dashed curve denotes the U.S.-Canadian border. The region below the curve is within the U.S.

measurements. Specifically, our setup performs better than a pure neutrino running option in combination with a short baseline detector, such as considered in Refs. [47,48]. We also checked that the medium energy beam option does not provide better sensitivities and would not significantly alter our conclusions.

In summary, we find that, for the mass hierarchy measurement, a longer baseline is preferable, whereas for $\sin^2 2\theta_{13}$ and *CP* violation the Ash River site does very well. In addition, it is not far from the optimum for the mass hierarchy. Since we do not find a satisfactory optimum for all performance indicators simultaneously, we choose Ash River for phase II; see Table II. Note that we will not use phase I for the comparisons (as for all of the other experiments). Since we have the same site for phase I and phase II and the luminosity for phase II is much higher, it does not significantly contribute to the sensitivities.

V. EXPERIMENTS WITH WIDE-BAND BEAMS

Wide-band beams are attractive because of their broad energy spectrum and higher on-axis flux [53,54]. A potential limitation of using water Cherenkov detectors with wide-band beams was thought to be the difficulty of isolating QE events from the NC background from the high-energy tail of the spectrum. Recent work using "Polfit," in conjunction with several other discriminants, has shown that adequate suppression of the π^0 background can be achieved [55]. Motivated by this significant development, a comprehensive analysis of an experiment with a 300 kt water Cherenkov detector was carried out in Ref. [35]. A LArTPC may be a promising alternative to reduce backgrounds very efficiently while having a higher efficiency through the utilization of non-QE events.

Currently, the most likely host for a wide-band beam in the U.S. is Fermilab. This leads to a number of interesting optimization issues. First, since the main injector (MI) can provide protons with energies between ~30 GeV and 120 GeV, where the maximum efficiency is reached at around 60 GeV, the proton energy needs to be optimized. Second, the proposed baseline from Fermilab to a deep underground science and engineering laboratory (DUSEL) at the Homestake or Henderson mines leads to additional constraints for the decay pipe since the boundaries of

Fermilab limit the decay pipe length. Compared to the NuMI beam which is pointed northerly and with a ~750 m decay tunnel, the Fermilab-Henderson southwesterly baseline would constrain the decay tunnel to less than 400 m. Therefore, one expects a different beam spectrum for these two cases. Third, choosing between the water Cherenkov and liquid argon detector technologies is an interesting issue. We will discuss these main optimization topics in Sec. V C. Note that, compared to the last section, we do not use a specific beam line and allow for arbitrary baseline-off-axis angle combinations. However, we work within the length constraints for a southwesterly directed decay tunnel. In some cases, we show the results for a northerly directed tunnel for comparison.

A. Simulation details

Our simulation is based on Ref. [35]. We use five years of neutrino running at 1 MW target power, and five years of antineutrino running at 2 MW target power. The baseline is 1290 km corresponding to Fermilab-Homestake. As a detector, we either use a 300 kt water Cherenkov detector or a 100 kt liquid argon TPC. Details of the LArTPC simulation are given in Sec. IV A, while details of the water Cherenkov detector simulation can be found in Ref. [35]. We use a systematic uncertainty of 5% on both signal and background. All of our setups are designed for the Fermilab MI as the proton source. As proton energies, we use 28 GeV corresponding to the old Brookhaven National Laboratory proposal, 60 GeV corresponding to the start of the maximum efficiency region, and 120 GeV corresponding to the current proton energy of the MI. All of these setups use the southwesterly pointed short decay tunnel. In addition, we show the results for 120 GeV protons and a new long northerly directed decay tunnel similar to the NuMI tunnel. For all setups, we use a LArTPC, but we compare it to the water Cherenkov detector for the 28 GeV protons. Our setups are summarized in Table I.

B. Motivation for on-axis operation

Before we address the main optimization issues for a WBB experiment, let us motivate the choice of baseline and off-axis angle, and compare the WBB to NOνA*. In Fig. 5, we show the performance for a hypothetical NOνA*

TABLE I. Different wide-band beam setups used in this section. The subscripts "S" and "L" indicate whether the decay tunnel is shorter or longer than 400 m.

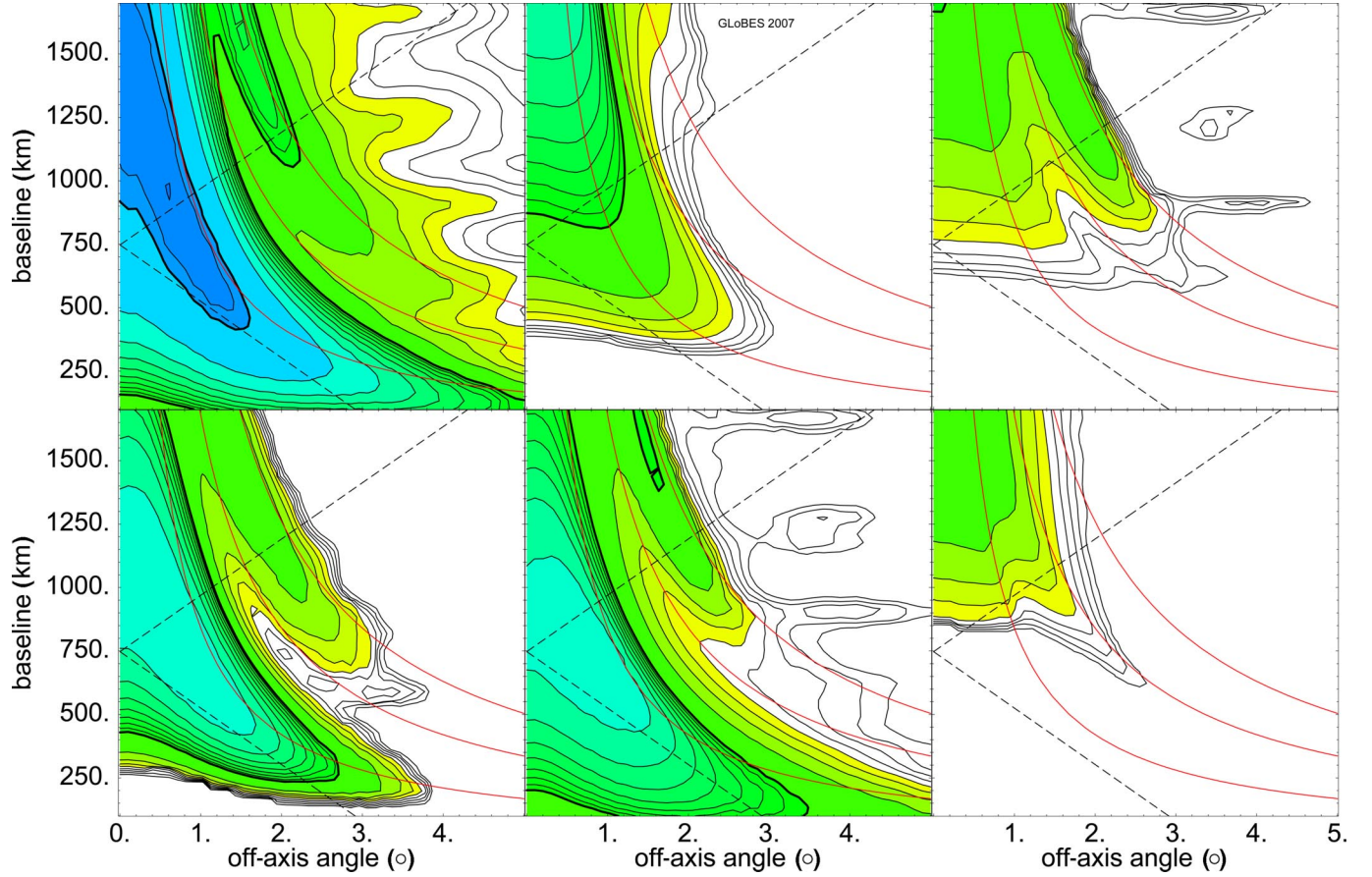| Setup	Proton energy	Detector technology	m_{det}	Decay tunnel Length	Direction
WBB-28$_S$-WC	28 GeV	Water Cherenkov	300 kt	Short	Southwesterly
WBB-28$_S$	28 GeV	LArTPC	100 kt	Short	Southwesterly
WBB-60$_S$	60 GeV	LArTPC	100 kt	Short	Southwesterly
WBB-120$_S$	120 GeV	LArTPC	100 kt	Short	Southwesterly
WBB-120$_L$	120 GeV	LArTPC	100 kt	Long	Northerly

FIG. 5 (color online). Optimization for a hypothetical NOνA* experiment (including phase I at Ash River) in the off-axis angle-baseline plane, but without being constrained by the NuMI beam line. Unlike Fig. 3, the full ranges for baselines and off-axis angles are shown. As in Fig. 3, the plots show the discovery reaches at the 3σ C.L. for nonzero $\sin^2 2\theta_{13}$, maximal CP violation, and the normal mass hierarchy. The thin black contours are logarithmically spaced in $\sin^2 2\theta_{13}$, i.e., $1, 2, \ldots, 9 \times 10^n$, where n ranges from -4 to -2. The color shading ranges from blue/dark (best) to green/light (worst); the bold contours correspond to $\sin^2 2\theta_{13} = 10^{-3}$ and 10^{-2}. The solid thin red curves are iso-L/E lines for the first, second, and third oscillation nodes. The constraints from the NuMI decay tunnel are shown as dashed lines for comparison.

experiment without constraints from the NuMI beam line, but for the same beam; i.e., we have allowed for the possibility of a new decay tunnel. The detector parameters and running times are those in Sec. IV. Note that detector locations within the dashed lines can be accommodated within the NuMI beam constraints. Unlike Fig. 3, the full ranges for baselines and off-axis angles are shown.

As can be seen from this figure, the choice of $L \simeq$ 1200–1500 km performs well for all measurements, and in (almost) all cases, at least as well as the best possible location with the NuMI decay tunnel constraint. In addition, there is no need to go off axis, because the NC rejection is assumed to be very efficient for the LArTPC. Note that the on-axis performance of even longer baselines has been studied in Ref. [35], and baselines between about 1200 and 1500 km were found to be optimal. Similarly, we find that the WBB on-axis concept with a baseline of ~1290 km in combination with a LArTPC is close to optimal for all performance indicators. Note that the

NuMI-like beam line and beam correspond to our wideband beam option WBB-120$_L$, i.e., the northerly directed decay tunnel. Compared to NOνA*, the detector is on axis and at a longer baseline.

C. Optimization of a Fermilab-based wide-band beam experiment

In order to discuss the impact of proton energy, decay pipe length, and detector technology, in Fig. 6, we show the $\sin^2 2\theta_{13}$, CP violation, and normal mass hierarchy discovery potentials of the WBB options in Table I. The performance of the setups improves as one moves down in Table I. Note that, for the option with a water Cherenkov detector, the exposure is a factor of 3 higher than the options with a LArTPC.

As far as the proton energy is concerned, compare the options WBB-28$_S$, WBB-60$_S$, and WBB-120$_S$, which are all for the same decay pipe length but for different proton
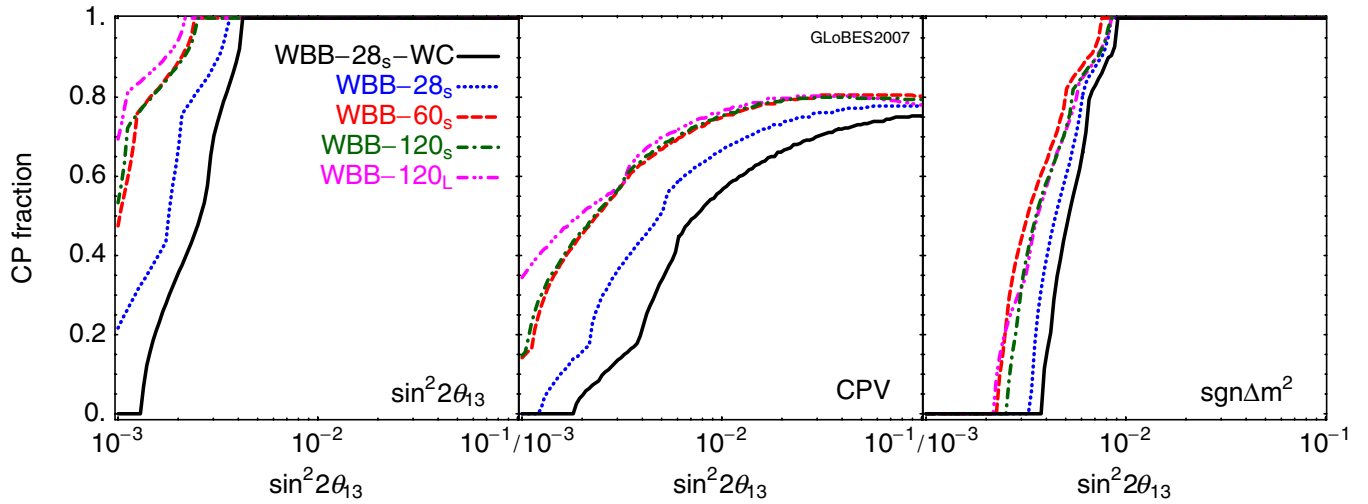
FIG. 6 (color online).   The 3σ discovery potentials for a nonzero $\sin^2 2\theta_{13}$, CP violation, and normal mass hierarchy of the WBB options in Table I.

energies. The performance improves with proton energy, but the WBB-60$_S$ setup is already close to optimum because the maximum efficiency (of the whole system) is reached for 60 GeV protons. A comparison of WBB-120$_S$ and WBB-120$_L$ indicates that the beam with the longer decay pipe performs better for small $\sin^2 2\theta_{13}$, which means that a NuMI-like beam is the best choice. However, Fermilab boundaries prohibit such a long decay pipe for the considered Fermilab-Homestake or -Henderson options, making WBB-120$_S$ the viable option. Note that a somewhat lower proton energy hardly has any impact on the physics performance, whereas a longer decay pipe could definitively help. To assess detector technologies, compare the WBB-28$_S$ (liquid argon) and WBB-28$_S$-WC setups. For the chosen detector masses of 100 kt for liquid argon and 300 kt for the water Cherenkov detector, respectively, the liquid argon setup performs significantly better. We find that 4 kt of water are equivalent to 1 kt of liquid argon for the $\sin^2 2\theta_{13}$ discovery, 4.4 kt of water are equivalent to 1 kt of liquid argon for the CP violation discovery, and 3.6 kt of water are equivalent to 1 kt of liquid argon for the mass hierarchy discovery. This means

that (at least for the 28 GeV proton energy) the cost per kt of water has to be less than 25% of the cost per kt of liquid argon in order to choose water as the detector material. Note that this ratio cannot be easily extrapolated to higher proton energies because of the higher neutrino energies and therefore higher NC background.

For the following physics comparison, we choose WBB-120$_S$.

VI. PHYSICS COMPARISON

In this section, we compare the chosen setups from each of the previous sections. In addition, we include a neutrino factory (NuFact) and a β-beam setup in some of the discussion. Our setups for this section are summarized in Table II.

A. Exposure scaling and normalized comparison

In order to compare the normalized performance of different experiments, in Fig. 7 we show the 3σ reaches for the discovery of nonzero $\sin^2 2\theta_{13}$, CP violation, and the normal hierarchy as functions of exposure. The dots

TABLE II.   Setups considered, neutrino t_ν and antineutrino $t_{\bar{\nu}}$ running times, corresponding target power P_{Target}, baseline L, detector technology, detector mass m_{det}, and exposure $\mathcal{L}$ [Mt MW 10^7 s]. For beta beam and NuFact, we assume 10^7 s of operation/year. Target power does not apply to an ion source used for the beta beam. We use 2.9×10^{18} useful ^{6}He decays/year and 1.1×10^{18} useful ^{18}Ne decays/year for the beta beam, where we have $\gamma = 350$ for both polarities. Details on the simulation can be found in Ref. [36]. For the neutrino factory, we use 10^{21} useful muon decays/year for both polarities, and two magnetized iron calorimeters at two different baselines. For details, see Refs. [34,37,38].

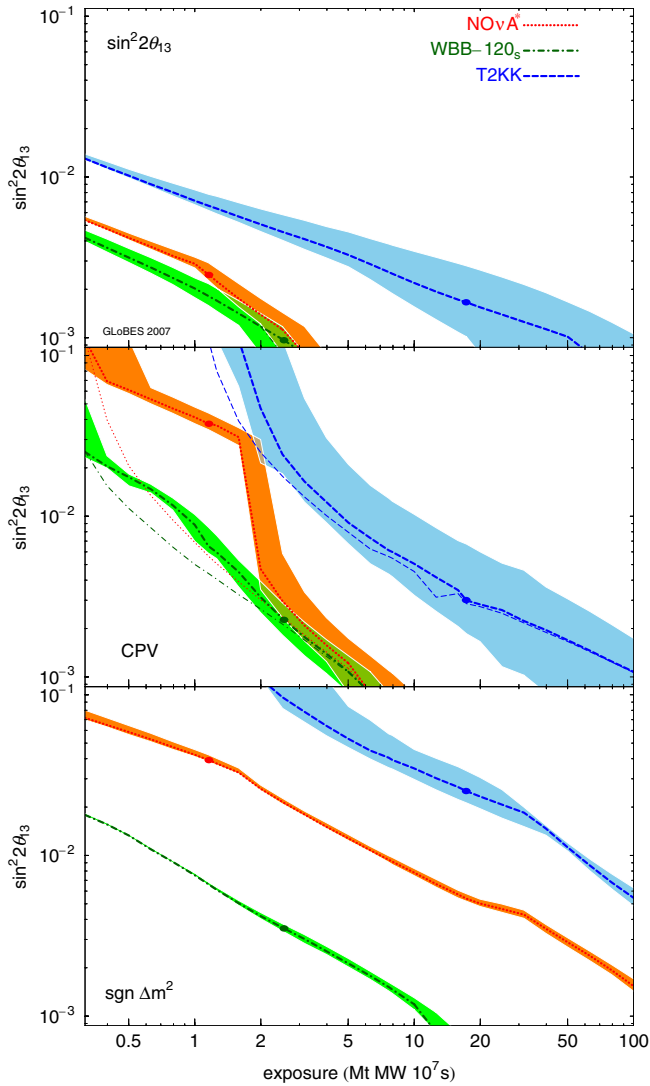| Setup	t_ν (yr)	$t_{\bar{\nu}}$ (yr)	P_{Target} (MW)	L (km)	Detector technology	m_{det} (kt)	$\mathcal{L}$
NOνA*	3	3	1.13($\nu/\bar{\nu}$)	810	LArTPC	100	1.15
WBB-120$_S$	5	5	1(ν) + 2($\bar{\nu}$)	1290	LArTPC	100	2.55
T2KK	4	4	4($\nu/\bar{\nu}$)	295 + 1050	Water Cherenkov	270 + 270	17.28
β-beam	4	4	$\cdots$	730	Water Cherenkov	500	$\cdots$
NuFact	4	4	4	3000 + 7500	Magnetized iron calor.	50 + 50	$\cdots$

FIG. 7 (color online). The $\sin^2 2\theta_{13}$ reach at 3σ for the discovery of nonzero $\sin^2 2\theta_{13}$, CP violation, and the normal hierarchy as a function of exposure. The curves are for a fraction of δ_{CP} of 0.5, which means that the performance will be better for 50% of all values of δ_{CP}, and worse for the other 50%. The light curves in the CPV panel are made under the assumption that the mass hierarchy is known to be normal. The dots mark the exposures of the setups as defined in Table II. The shaded regions result by varying the systematic uncertainties from 2% (lower edge) to 10% (upper edge).

mark the nominal exposures of the setups as given in Table II. The shaded regions show the dependence of the sensitivities on the level of systematic uncertainties. The lower (upper) edge of each region corresponds to a systematic uncertainty of 2% (10%). Observe that the detection of CP violation is more sensitive to the systematic uncertainty than the other measurements.

Most of the discovery reaches in Fig. 7 scale more or less like statistics, where there may be a slight transition from rate to spectrum dominated regimes (see, for instance, CPV

for T2KK). The only severe exception is the NOνA* scaling of the CPV reach, which was noticed and explained in Ref. [13]. In this case, a slightly higher luminosity can have a tremendous impact by the resolution of the mass hierarchy degeneracy (cf. light curves for known mass hierarchy). A factor of 2 higher luminosity could increase the $\sin^2 2\theta_{13}$ reach by an order of magnitude.

NOνA* and WBB-120$_S$ are approximately equal concepts for large enough exposures $\gtrsim 2$ Mt MW 10^7 s for the $\sin^2 2\theta_{13}$ and CP violation discoveries. However, for the mass hierarchy discovery, WBB-120$_S$ performs better because of the longer baseline. The curves for the T2KK concept are all above the ones for the Fermilab-based setups. In this case, one has to take into account the lower cost of water compared to liquid argon as detector material. However, the lower neutrino energies and the low event rates in the detector in Korea highly affect the competitiveness. One can also see these properties in the event rate spectra for the same exposure in Fig. 8. The NOνA* and WBB-120$_S$ options have broader spectra that peak at higher energies, and the integrated event rate is much higher.

B. Prediction for nominal exposure and its robustness

We compare in Fig. 9 the absolute performance for the exposures given in Table II. For all performance indicators, the WBB-120$_S$ has the strongest physics potential and NOνA* the weakest. All experiments can discover $\sin^2 2\theta_{13}$, CP violation, and the mass hierarchy for large $\sin^2 2\theta_{13}$ for most values of δ_{CP}, but there are substantial differences for smaller values of $\sin^2 2\theta_{13}$. As we have seen above, this performance comparison changes on normalizing the exposure.

Let us assess how robust the conclusions based on the nominal exposure are under the following three main impact factors which could affect the performance of a superbeam upgrade:

(1) The originally anticipated luminosity cannot be reached, or an improvement of the proton plan leads to a substantial increase of the originally anticipated luminosity. To account for this possibility, we vary the exposure between half and twice the exposure we have used so far.

(2) The original systematic error estimate turns out to be too optimistic or too conservative. We vary the signal and background normalization errors between 2% and 10%. We have assumed a 5% uncertainty throughout.

(3) The current best-fit value of Δm_{31}^2 that the experiments are optimized for turns out to be somewhat different from the actual value. We vary Δm_{31}^2 between 2.0×10^{-3} eV^2 and 3.0×10^{-3} eV^2.

The results of this robustness analysis are displayed in Fig. 10. Each bar reflects the range from a too conservative original estimate (left end) to the original assumption (bold
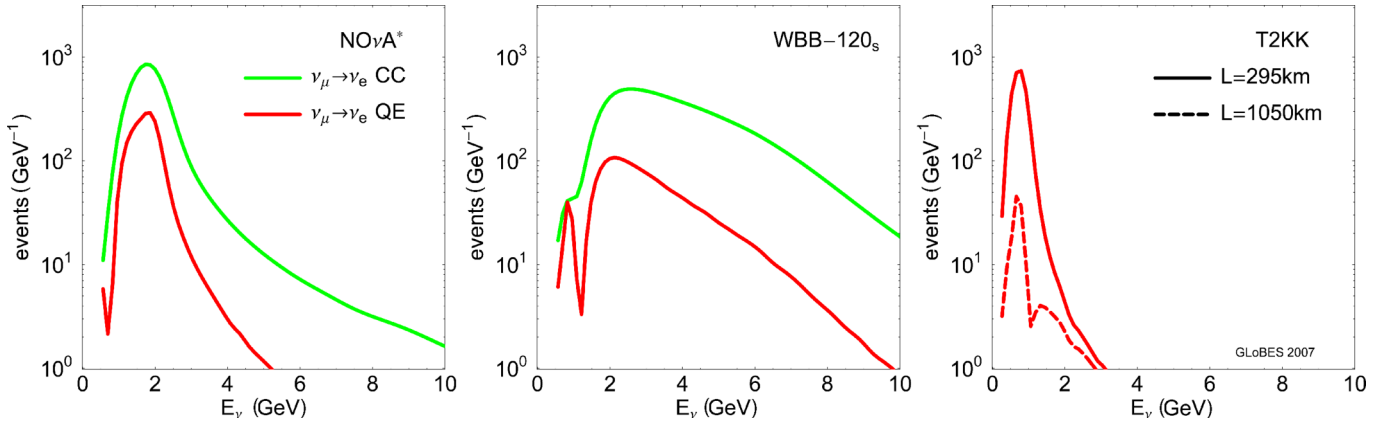
FIG. 8 (color online). Neutrino event rate spectra for $\sin^2 2\theta_{13} = 0.04$, $\delta_{CP} = 0$ for NOνA*, WBB-120$_S$, and T2KK. All spectra are computed for an exposure of 1 Mt MW 10^7 s including detection efficiencies and energy resolution. For NOνA* and WBB, red/dark curves are the QE events only, and the green/light curves are the non-QE events only. For T2KK, the solid curve refers to the detector in Japan, the dashed curve to the detector in Korea.
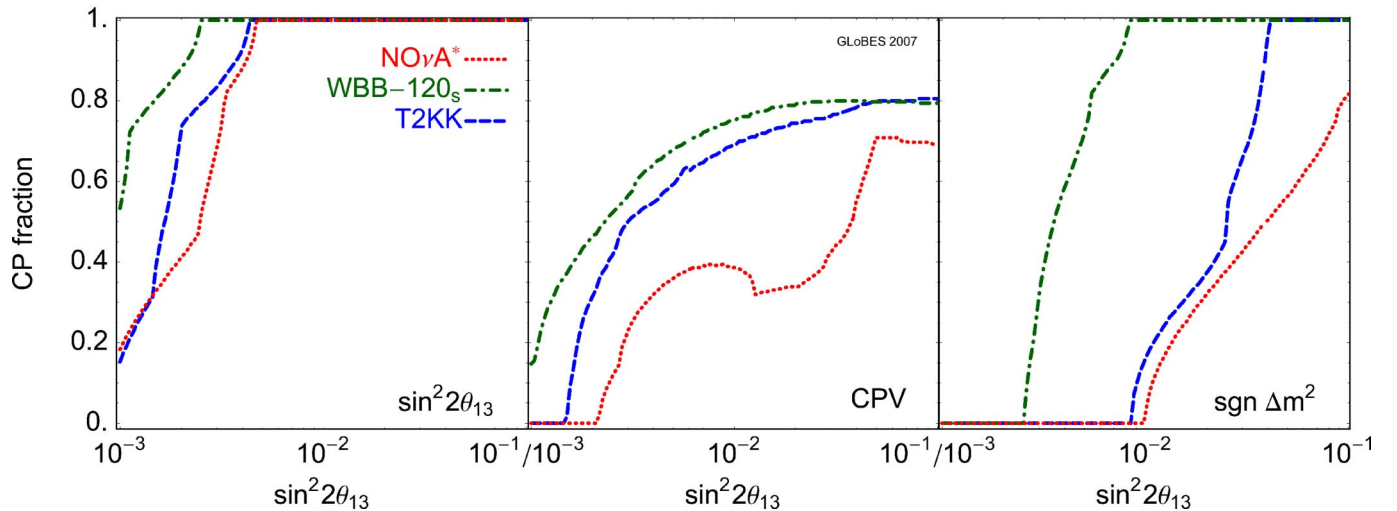

FIG. 9 (color online). Comparison of superbeam upgrades in the configurations of Table II at the 3σ C.L. The plots show the discovery reaches for a nonzero $\sin^2 2\theta_{13}$, CP violation, and the normal hierarchy.

vertical lines) to a too optimistic original estimate (right end).

From the upper row of the CPV panel, we see that a factor of 2 higher luminosity for NOνA* leads to a much better CP violation performance. The impact of an incorrect systematics estimate is strongest on T2KK and weakest on NOνA*. Experiments using a LArTPC are much less sensitive to variations of the systematic errors since the background levels are much lower. This also implies that T2KK has the most to gain from a better understanding of systematics. On the other hand, increasing the systematics from 5% to 10% in T2KK would require us to increase the exposure by nearly a factor 3 to compensate the loss of sensitivity to nonzero $\sin^2 2\theta_{13}$ and δ_{CP}. The sensitivity of experiments with narrow-band beams, NOνA* and T2KK, is very much affected by the actual value of Δm_{31}^2, whereas the sensitivity of WBB-120$_S$ is hardly affected. Note that, in this case, we observe the strongest impact on NOνA*.

The ranges covered by the bars provide a measure of risk. Since the bars for the $\sin^2 2\theta_{13}$ and CP violation discoveries overlap for the different setups, they may yield very similar results given their nominal exposures. Only for the mass hierarchy measurement is WBB-120$_S$ significantly better than the other two experiments.

Another important consideration is the effect of the octant degeneracy which appears for deviations of θ_{23} from $\pi/4$. In Fig. 11, we show the sensitivities of each setup under the assumption that $\theta_{23} = 0.664$ or 0.927, which are at the extremes of the 2σ interval allowed by atmospheric data. So long as θ_{23} does not deviate substantially from $\pi/4$, and become inconsistent with current data, this degeneracy does not affect our results significantly. All experiments besides NOνA* show a simple rescaling of their sensitivities. For NOνA*, the wrong-octant, wrong-hierarchy solution impacts the CPV and the mass hierarchy measurements.
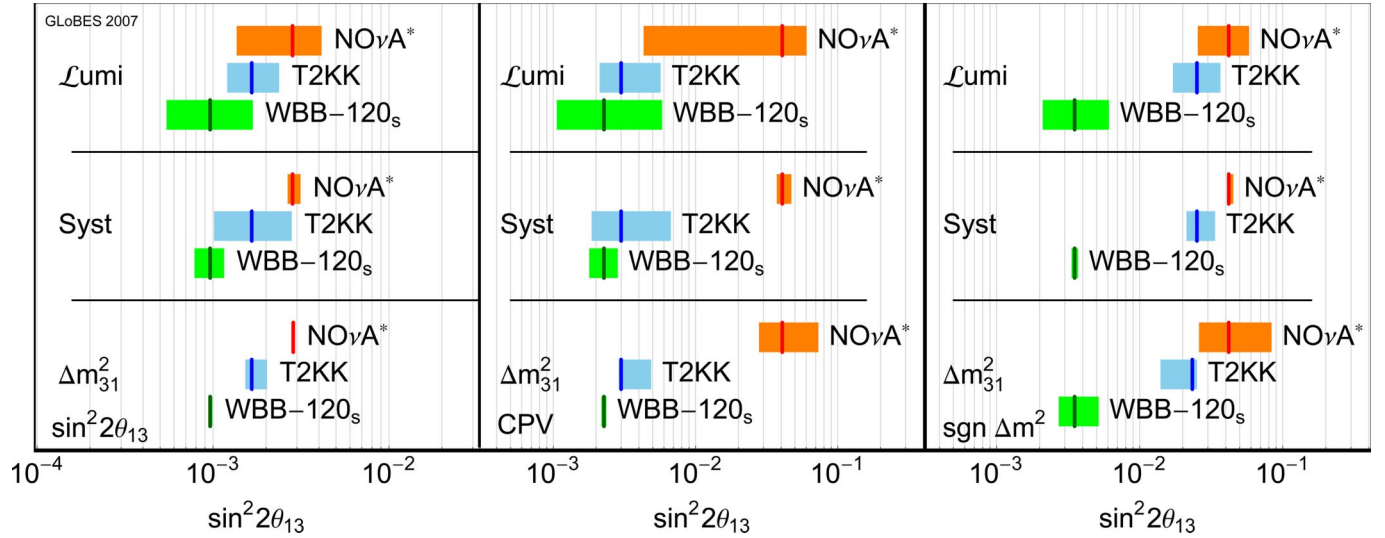
FIG. 10 (color online). Robustness with respect to the main impact factors, luminosity/exposure, systematics prediction, and true Δm_{31}^2. We show the impact on the 3σ reaches for a nonzero $\sin^2 2\theta_{13}$, CP violation, and the mass hierarchy, assuming a CP fraction of 0.5. The bold vertical lines within the bars correspond to our standard assumptions. The bars mark the ranges between the best case assumptions (double exposure, 2% systematic errors, $\Delta m_{31}^2 = 3.0 \times 10^{-3}$ eV^2) and the worst case assumptions (half exposure, 10% systematic errors, $\Delta m_{31}^2 = 2.0 \times 10^{-3}$ eV^2) for the respective impact factor.
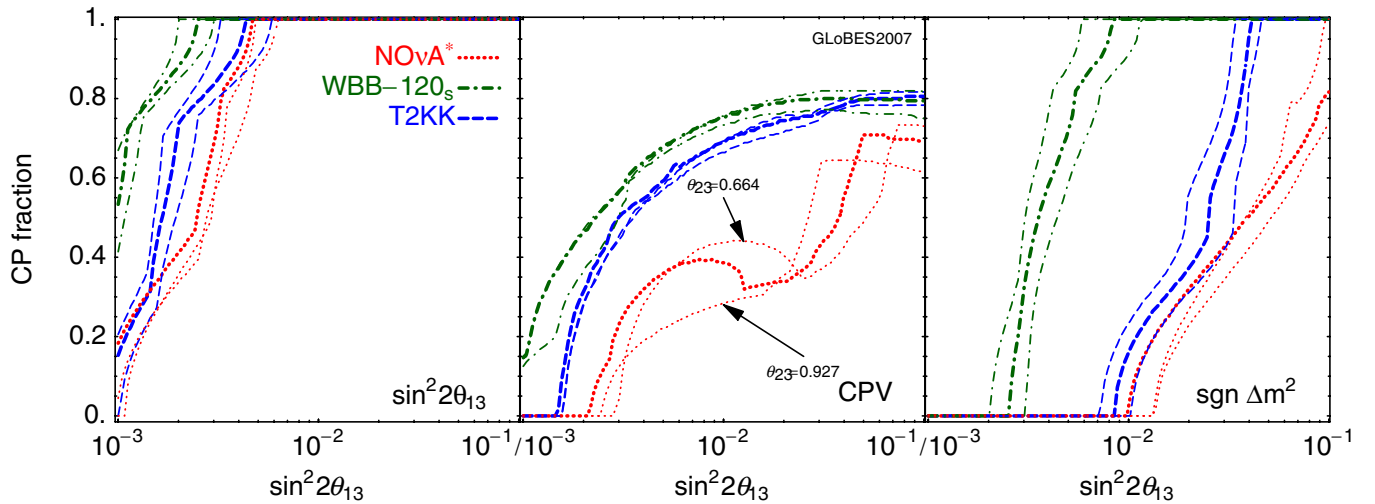

FIG. 11 (color online). Effect of the octant degeneracy on the 3σ sensitivities of the experiments. The three sets of curves for each experiment correspond to $\theta_{23} = 0.664$, $\pi/4$ (thick lines) and 0.927. Other than for NOνA* (for which a degenerate solution limits the sensitivities), the naive expectation that the sensitivities are greater for larger θ_{23} is borne out.

Finally, we consider how assumptions about the energy resolution affect our results. Spectral information is relevant only when statistics are large, i.e., when θ_{13} is large. For small θ_{13} the energy resolution is of little relevance since spectral information does not enhance the sensitivity. The energy resolution of the water Cherenkov detector is based on a simulation of the Super-Kamiokande detector [55]. For the options using a LArTPC, the energy resolution is more uncertain. We explicitly checked that, for $\sin^2 2\theta_{13} = 0.1$, varying the energy resolution for QE events between $5\%/\sqrt{E}$ and $20\%/\sqrt{E}$ barely affects the fraction of CP phases for which a given measurement can

be performed. The typical variation is less than 0.01. The only exception occurs for the determination of the mass hierarchy with NOνA*, for which the CP fraction changes from 0.84 at $5\%/\sqrt{E}$ to 0.72 at $20\%/\sqrt{E}$.

C. Comparison with a neutrino factory and a β-beam experiment

For small $\sin^2 2\theta_{13} \ll 10^{-2}$, it is well known that a neutrino factory complex has the optimal physics potential for all of the considered performance indicators (cf., e.g., Ref. [38]). This is a consequence of the high neutrino
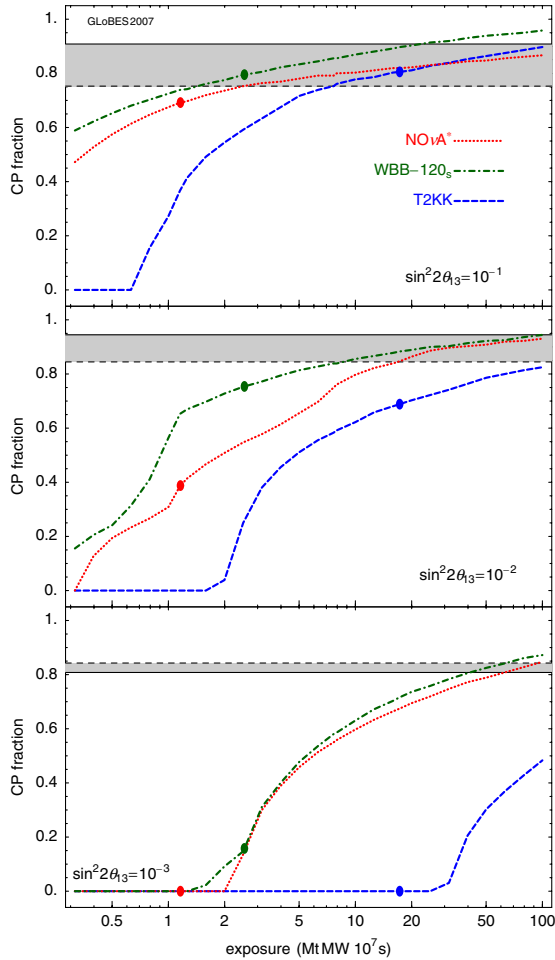
FIG. 12 (color online). *CP* fraction for a 3σ discovery of *CP* violation as a function of exposure. The different panels correspond to $\sin^2 2\theta_{13} = 0.1$, $\sin^2 2\theta_{13} = 0.01$, and $\sin^2 2\theta_{13} = 0.001$. The shaded region marks the potential between a β-beam (solid line) and neutrino factory (dashed line) as defined in Table II.

energies and high event rates. However, the oscillation maximum sits at relatively low energies, where the backgrounds from event misidentification are large, and the event rates are comparatively moderate. Therefore, for large $\sin^2 2\theta_{13}$, a β-beam or superbeam experiment tuned to the oscillation maximum may have the better performance. Since the effort for a β-beam may be larger than for a superbeam upgrade, and the technology needs further exploration, it is an interesting question if the superbeam upgrades can compete with a neutrino factory or β-beam for large $\sin^2 2\theta_{13}$. We use the neutrino factory and β-beam setups from Table II for this comparison.[4]

---

[4]Note that some gain in the neutrino factory or β-beam performance can be obtained by a reoptimization for large $\sin^2 2\theta_{13}$ (see, e.g., Refs. [38,56,57]). However, this gain is usually moderate.

All the experiments under consideration have good sensitivity to nonzero $\sin^2 2\theta_{13}$ and the mass hierarchy for large $\sin^2 2\theta_{13}$. We therefore do not discuss the $\sin^2 2\theta_{13}$ and mass hierarchy sensitivities and focus on the *CP* violation measurement.

In Fig. 12 we show the *CP* fraction for the 3σ discovery of *CP* violation as a function of exposure. The different panels correspond to different true values of $\sin^2 2\theta_{13}$. The shaded region marks the potential between a β-beam (solid line) and neutrino factory (dashed line) as given in Table II. For $\sin^2 2\theta_{13} = 0.1$, the superbeam upgrades perform at least as well as the neutrino factory, and a moderate increase of exposure can make their physics potential optimal. Note that, for instance, the neutrino factory requires a target power of 4 MW. The Fermilab-based experiments therefore still have space for an increase of target power. For $\sin^2 2\theta_{13} = 0.01$, the situation is already very different. In this case, WBB-120$_S$ can compete with the neutrino factory with a factor of 2 or 3 increase in the exposure. This upgrade basically corresponds to an upgraded proton source and a somewhat longer running time. The increase in exposure necessary for NOνA* and T2KK to be competitive is unrealistic. For $\sin^2 2\theta_{13} = 0.001$, experiments with upgraded superbeams cease to be competitive.

The above discussion indicates that superbeams may be the technology of choice for large $\sin^2 2\theta_{13}$. However, if $\sin^2 2\theta_{13}$ is not discovered in the coming generation of superbeam and reactor experiments, one will have to consider a neutrino factory or β-beam optimized for a maximum reach in $\sin^2 2\theta_{13}$.

VII. SUMMARY

The important points of our paper that address the goals listed in the introduction are as follows:

(1) T2KK: Placing half the fiducial mass of the detector at 1050 km improves the sensitivity to the mass hierarchy and to *CP* violation. Using identical detectors at the 1050 km and 295 km baselines so that the systematics are fully correlated only improves the sensitivity to the mass hierarchy.

(2) The optimal location for a NOνA* detector within the U.S. is the Ash River site. Better risk-minimized mass hierarchy and *CP* violation sensitivities can be obtained with a baseline ∼880–930 km.

(3) The optimal baseline for a wide-band beam experiment is between 1200 and 1500 km. High proton energies and a long decay tunnel are preferable.

(4) Among experiments with super neutrino beams, wide-band beam experiments have the most robust performance and the best mass hierarchy performance. The sensitivity of experiments with narrow-band beams is significantly affected by the true value of $|\Delta m_{31}^2|$. Overall, wide-band beam experiments are the best experimental concept.

(5) NOνA* is competitive with WBB-120$_S$ for the discovery of nonzero θ_{13} and *CP* violation for exposures above 2 Mt MW 10^7 s.

(6) Within the context of wide-band beam experiments, approximately 4 t of water performs as well as 1 t of liquid argon. However, this ratio may be different for proton energies higher than 28 GeV.

(7) Superbeam versus β-beam/NuFact: WBB-120$_S$ is a better experimental concept than a neutrino factory if $\sin^2 2\theta_{13} \gtrsim 0.01$. For $\sin^2 2\theta_{13} \lesssim 0.01$, experiments with superbeams are not competitive. For the exposures listed in Table II, if

  (a) $\sin^2 2\theta_{13} \gtrsim 0.04$: T2KK or WBB-120$_S$ can make all three measurements with similar sensitivities as a β-beam/NuFact.

  (b) $0.01 \lesssim \sin^2 2\theta_{13} \lesssim 0.04$: Only WBB-120$_S$ performs as well as a β-beam/NuFact. T2KK is unable to establish the mass hierarchy with equivalent sensitivity.

ACKNOWLEDGMENTS

APPENDIX: MORE DETAILS ON THE OPTIMIZATION OF NOνA*

In Tables III, IV, and V we list all sites which have optimal sensitivity in at least one of the six cases $\delta_{CP} = \pm 90°$ and $\Delta m_{31}^2 = (2.0, 2.5, 3.0) \times 10^{-3}$ eV^2 for at least one of our performance indicators, and we show the actual sensitivity reaches. The geographical location of those sites is shown in Fig. 13. What this figure demonstrates is that the Ash River site is the best possible choice within the U.S. and is not far from the optimum configuration. However, note that many of the optimal locations are on Canadian soil, especially for the determination of the mass hierarchy.

TABLE III. Relative sensitivity reach at 3σ for $\delta_{CP} = \pm 90°$ and $\Delta m_{31}^2 = 2.0 \times 10^{-3}$ eV^2 for various sites defined by off-axis angle (OA) and baseline (L). The 18 sites in this table have been identified to be optimal for one specific measurement and one choice of $\delta_{CP} = \pm 90°$ and $\Delta m_{31}^2 = (2.0, 2.5, 3.0) \times 10^{-3}$ eV^2. The third row contains the absolute value of $\sin^2 2\theta_{13}$ which was achieved at the best site for that case. "n.s." denotes no sensitivity for $\sin^2 2\theta_{13} < 0.1$. The absolute sensitivity in $\sin^2 2\theta_{13}$ can be obtained by multiplying each column with the value of $\sin^2 2\theta_{13}^{\text{opt}}$ in that column. The last row labeled AR denotes the Ash River sites.

	Site		$\sin^2 2\theta_{13}$		CPV		sgnΔm^2	
	OA (o)	L (km)	$+90°$	$-90°$	$+90°$	$-90°$	$+90°$	$-90°$
$\sin^2 2\theta_{13}^{\text{opt}}[10^{-3}]$			0.91	2.47	10.95	2.23	41.36	55.4
1	0.91	910	1.00	1.00	1.10	1.03	1.39	n.s.
2	1.02	806	1.04	1.00	1.37	1.05	1.95	n.s.
3	1.03	975	1.11	1.19	1.00	1.18	1.14	n.s.
4	1.14	806	1.04	1.04	1.35	1.00	1.89	n.s.
5	1.25	1025	1.77	2.50	1.08	4.97	1.00	1.75
6	1.7	1126	15.90	28.70	2.47	21.80	1.75	1.00
7	0.62	884	1.09	1.06	1.23	1.19	1.56	n.s.
8	0.68	832	1.11	1.06	1.36	1.18	1.85	n.s.
9	0.91	949	1.00	1.03	1.03	1.04	1.25	n.s.
10	0.68	780	1.19	1.13	1.58	1.24	2.29	n.s.
11	1.93	1176	27.00	15.00	5.89	21.80	1.25	1.39
12	1.36	1050	2.63	4.67	1.16	8.61	1.01	1.47
13	0.57	858	1.14	1.13	1.33	1.25	1.70	n.s.
14	0.23	798	1.59	1.52	1.70	1.51	2.22	n.s.
15	0.68	899	1.05	1.00	1.17	1.13	1.48	n.s.
16	0.68	666	1.42	1.47	2.29	1.46	n.s.	n.s.
17	1.7	1126	15.90	28.70	2.47	21.80	1.75	1.00
18	1.14	1000	1.28	1.54	1.01	1.56	1.03	n.s.
AR	0.89	810	1.07	1.03	1.41	1.13	1.98	n.s.

TABLE IV.   Similar to Table III but for $\Delta m_{31}^2 = 2.5 \times 10^{-3}$ eV^2.

| | Site | | $\sin^2 2\theta_{13}$ | | CPV | | sgnΔm^2 | |
	OA (o)	L (km)	+90°	−90°	+90°	−90°	+90°	−90°
$\sin^2 2\theta_{13}^{\mathrm{opt}}[10^{-3}]$			0.81	2.13	8.16	2.37	12.19	34.01
1	0.91	910	1.13	1.30	1.05	1.46	2.45	1.28
2	1.02	806	1.13	1.22	1.26	1.26	3.38	n.s.
3	1.03	975	1.60	2.23	1.04	3.29	2.28	1.38
4	1.14	806	1.27	1.49	1.31	1.69	3.26	n.s.
5	1.25	1025	4.18	9.28	1.30	8.11	2.59	1.11
6	1.7	1126	16.90	9.88	7.23	9.26	1.96	1.82
7	0.62	884	1.00	1.03	1.09	1.06	2.85	1.36
8	0.68	832	1.02	1.00	1.19	1.02	3.24	2.94
9	0.91	949	1.19	1.45	1.00	1.77	2.28	1.10
10	0.68	780	1.04	1.01	1.34	1.00	3.81	n.s.
11	1.93	1176	10.20	6.32	9.69	4.92	1.00	2.75
12	1.36	1050	7.95	16.60	1.70	11.10	3.48	1.00
13	0.57	858	1.01	1.04	1.16	1.05	3.07	1.53
14	0.23	798	1.37	1.27	1.44	1.15	3.73	n.s.
15	0.68	899	1.00	1.03	1.05	1.08	2.74	1.30
16	0.68	666	1.16	1.13	1.81	1.04	5.86	n.s.
17	1.7	1126	16.90	9.88	7.23	9.26	1.96	1.82
18	1.14	1000	2.32	4.08	1.12	5.39	2.33	1.29
AR	0.89	810	1.03	1.06	1.24	1.07	3.46	2.91

TABLE V.   Similar to Table III but for $\Delta m_{31}^2 = 3.0 \times 10^{-3}$ eV^2.

| | Site | | $\sin^2 2\theta_{13}$ | | CPV | | sgnΔm^2 | |
	OA (o)	L (km)	+90°	−90°	+90°	−90°	+90°	−90°
$\sin^2 2\theta_{13}^{\mathrm{opt}}[10^{-3}]$			0.75	1.85	6.53	2.24	8.03	21.98
1	0.91	910	1.57	2.32	1.08	2.86	2.68	1.28
2	1.02	806	1.55	2.10	1.30	2.53	3.48	2.03
3	1.03	975	2.92	5.40	1.17	5.13	2.59	1.06
4	1.14	806	2.03	3.25	1.42	3.77	3.62	2.16
5	1.25	1025	9.95	11.30	2.39	9.63	3.14	1.17
6	1.7	1126	7.13	4.79	9.23	3.47	1.00	3.29
7	0.62	884	1.04	1.23	1.02	1.30	2.63	1.01
8	0.68	832	1.05	1.19	1.11	1.23	3.06	1.25
9	0.91	949	1.75	2.77	1.05	3.33	2.51	1.12
10	0.68	780	1.03	1.12	1.23	1.11	3.59	1.53
11	1.93	1176	10.50	13.30	9.69	14.70	6.12	4.28
12	1.36	1050	14.10	9.04	4.48	9.80	2.87	1.68
13	0.57	858	1.00	1.16	1.07	1.18	2.87	1.13
14	0.23	798	1.25	1.00	1.31	1.10	3.61	1.48
15	0.68	899	1.10	1.32	1.00	1.47	2.46	0.94
16	0.68	666	1.06	0.91	1.58	1.00	5.04	n.s.
17	1.7	1126	7.13	4.79	9.23	3.47	1.00	3.29
18	1.14	1000	5.16	9.62	1.44	7.25	2.95	1.00
AR	0.89	810	1.18	1.43	1.20	1.57	3.21	1.48
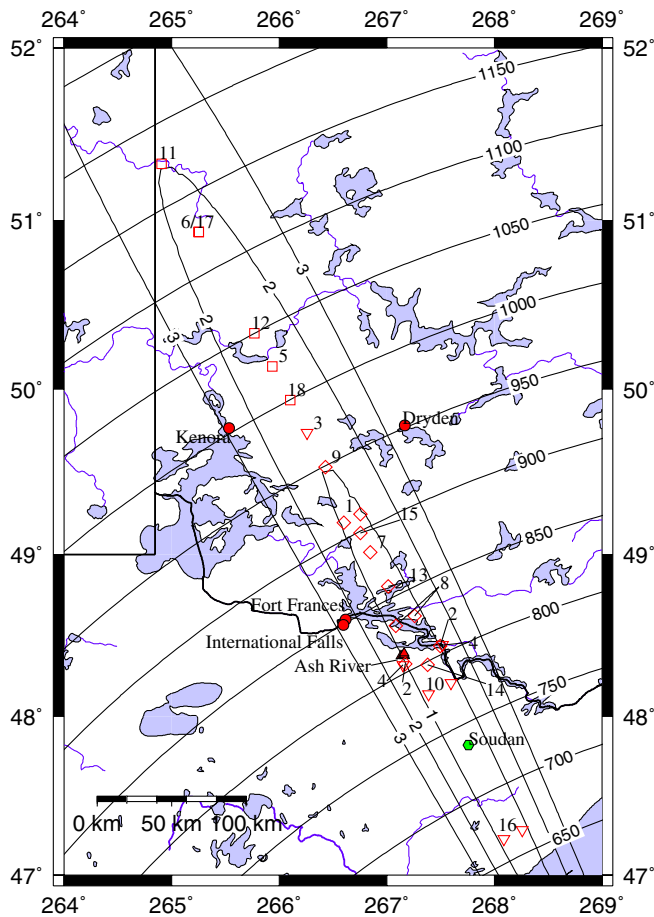
FIG. 13 (color online). Location of the points with optimal sensitivity reach in $\sin^2 2\theta_{13}$. Shown are all the optima for $\delta_{CP} = \pm 90°$ and $\Delta m_{31}^2 = (2.0, 2.5, 3.0) \times 10^{-3}$ eV^2. Red diamonds mark the points for the discovery of $\sin^2 2\theta_{13}$, inverted red triangles mark the points for CP violation, and red squares mark the points for discovery of the normal mass hierarchy. The numbers refer to the sites in Tables III, IV, and V where the actual achievable sensitivities are listed. The upright red filled triangles denote the six possible NOνA sites given in [45]. The contours denote places with the same off-axis angle (ellipses) in degrees and with the same baseline from Fermilab (circles) in km. The thick black curve is the U.S./Canadian border. The map is a Mercator projection.

[1] R. N. Mohapatra and A. Y. Smirnov, Annu. Rev. Nucl. Part. Sci. **56**, 569 (2006).

[2] E. Ables *et al.* (MINOS), Report No. FERMILAB-PROPOSAL-0875.

[3] V. D. Barger *et al.*, Phys. Rev. D **65**, 053016 (2002).

[4] P. Huber, M. Lindner, M. Rolinec, T. Schwetz, and W. Winter, Phys. Rev. D **70**, 073014 (2004).

[5] F. Ardellier *et al.* (Double CHOOZ), arXiv:hep-ex/0606025.

[6] X. Guo *et al.* (Daya Bay), arXiv:hep-ex/0701029.

[7] P. Huber, J. Kopp, M. Lindner, M. Rolinec, and W. Winter, J. High Energy Phys. 05 (2006) 072.

[8] Y. Itow *et al.*, Nucl. Phys. B, Proc. Suppl. **111**, 146 (2001).

[9] V. Barger, D. Marfatia, and K. Whisnant, Int. J. Mod. Phys. E **12**, 569 (2003).

[10] M. Ishitsuka, T. Kajita, H. Minakata, and H. Nunokawa, Phys. Rev. D **72**, 033003 (2005).

[11] K. Hagiwara, N. Okamura, and K.-i. Senda, Phys. Lett. B **637**, 266 (2006).

[12] T. Kajita, H. Minakata, S. Nakayama, and H. Nunokawa, Phys. Rev. D **75**, 013006 (2007).

[13] V. Barger, P. Huber, D. Marfatia, and W. Winter, Phys. Rev. D **76**, 031301 (2007).

[14] V. Barger, D. Marfatia, and K. Whisnant, Phys. Rev. D **65**, 073023 (2002).

[15] J. Burguet-Castell, M. B. Gavela, J. J. Gomez-Cadenas, P. Hernandez, and O. Mena, Nucl. Phys. **B608**, 301 (2001).

[16] H. Minakata and H. Nunokawa, J. High Energy Phys. 10 (2001) 001.

[17] G. L. Fogli and E. Lisi, Phys. Rev. D **54**, 3667 (1996).

[18] V. D. Barger, K. Whisnant, S. Pakvasa, and R. J. N. Phillips, Phys. Rev. D **22**, 2718 (1980).

[19] H. Minakata, H. Nunokawa, and S. J. Parke, Phys. Rev. D **66**, 093012 (2002).

[20] H. Minakata, H. Nunokawa, and S. J. Parke, Phys. Lett. B **537**, 249 (2002).

[21] H. Minakata, H. Nunokawa, and S. J. Parke, Phys. Rev. D **68**, 013010 (2003).

[22] W. Winter, Phys. Rev. D **70**, 033006 (2004).

[23] P. Huber, M. Lindner, and W. Winter, Comput. Phys. Commun. **167**, 195 (2005); http://www.mpi-hd.mpg.de/lin/globes/

[24] P. Huber, J. Kopp, M. Lindner, M. Rolinec, and W. Winter, Comput. Phys. Commun. **177**, 432 (2007).

[25] M. Maltoni, T. Schwetz, M. A. Tortola, and J. W. F. Valle, New J. Phys. **6**, 122 (2004).

[26] T. Schwetz, Phys. Scr. **T127**, 1 (2006).

[27] H. Minakata, H. Nunokawa, W. J. C. Teves, and R. Zukanovich Funchal, Phys. Rev. D **71**, 013005 (2005).

[28] A. Bandyopadhyay, S. Choubey, S. Goswami, and S. T. Petcov, Phys. Rev. D **72**, 033013 (2005).

[29] S. Antusch, P. Huber, J. Kersten, T. Schwetz, and W. Winter, Phys. Rev. D **70**, 097302 (2004).

[30] R. J. Geller and T. Hara, Nucl. Instrum. Methods Phys. Res., Sect. A **503**, 187 (2003).

[31] T. Ohlsson and W. Winter, Phys. Rev. D **68**, 073007 (2003).

[32] K. Hagiwara, N. Okamura, and K.-i. Senda, arXiv:hep-ph/0607255.

[33] K. Hagiwara and N. Okamura, arXiv:hep-ph/0611058.

[34] P. Huber, M. Lindner, and W. Winter, Nucl. Phys. **B645**, 3 (2002).

[35] V. Barger *et al.*, Phys. Rev. D **74**, 073004 (2006).

[36] J. Burguet-Castell, D. Casper, E. Couce, J. J. Gomez-Cadenas, and P. Hernandez, Nucl. Phys. **B725**, 306 (2005).

[37] P. Huber and W. Winter, Phys. Rev. D **68**, 037301 (2003).

[38] P. Huber, M. Lindner, M. Rolinec, and W. Winter, Phys. Rev. D **74**, 073003 (2006).

[39] D. G. Michael *et al.* (MINOS), Phys. Rev. Lett. **97**, 191801 (2006).

[40] D. Ayres *et al.*, arXiv:hep-ex/0210005.

[41] V. Barger, D. Marfatia, and K. Whisnant, Phys. Rev. D **66**, 053007 (2002).

[42] V. Barger, D. Marfatia, and K. Whisnant, Phys. Lett. B **560**, 75 (2003).

[43] P. Huber, M. Lindner, and W. Winter, Nucl. Phys. **B654**, 3 (2003).

[44] O. Mena, H. Nunokawa, and S. J. Parke, Phys. Rev. D **75**, 033002 (2007).

[45] D. S. Ayres *et al.* (NOνA), arXiv:hep-ex/0503053.

[46] M. G. Albrow *et al.*, arXiv:hep-ex/0509019.

[47] O. Mena Requejo, S. Palomares-Ruiz, and S. Pascoli, Phys. Rev. D **72**, 053002 (2005).

[48] O. Mena, S. Palomares-Ruiz, and S. Pascoli, Phys. Rev. D **73**, 073007 (2006).

[49] R. M. Zwaska, Fermilab Proton Projections for Long-Baseline Neutrino Beams, Technical Report Beams Document 2393-v1, FNAL (2006).

[50] M. Messier, http://enrico1.physics.indiana.edu/messier/off-axis/spectra/.

[51] B. Fleming (private communication).

[52] M. D. Messier (private communication).

[53] D. Beavis *et al.*, arXiv:hep-ex/0205040.

[54] M. V. Diwan *et al.*, Phys. Rev. D **68**, 012002 (2003).

[55] C. Yanagisawa, C. Jung, P. T. Lee, and B. Viren, report submitted to The U.S. Long Baseline Neutrino Experiment Study, http://nwg.phy.bnl.gov/~diwan/nwg/fnal-bnl/docs/numunuePREBWv3.pdf.

[56] P. Huber, M. Lindner, M. Rolinec, and W. Winter, Phys. Rev. D **73**, 053002 (2006).

[57] S. Geer, O. Mena, and S. Pascoli, Phys. Rev. D **75**, 093001 (2007).